J Mar Sci Technol (2010) 15:1–15
DOI 10.1007/s00773-009-0066-1

ORIGINAL ARTICLE

Strength and deformability of corroded steel plates under quasi-static tensile load

Md. Mobesher Ahmmad · Y. Sumi

Received: 25 April 2009 / Accepted: 2 August 2009 / Published online: 10 September 2009

Abstract The objective of this study was to estimate the strength and deformability of corroded steel plates under quasi-static uniaxial tension. In order to accurately simulate this problem, we first estimated the true stress–strain relationship of a flat steel plate by introducing a vision sensor system to the deformation measurements in tensile tests. The measured true stress–stain relationship was then applied to a series of nonlinear implicit three-dimensional finite element analyses using commercial code LS-DYNA. The strength and deformability of steel plates with various pit sizes, degrees of pitting intensity, and general corrosion were estimated both experimentally and numerically. The failure strain in relation to the finite element mesh size used in the analyses was clarified. Two different steels having yield ratios of 0.657 and 0.841 were prepared to examine the material effects on corrosion damage. The strength and deformability did not show a clear dependence on the yield ratios of the present two materials, whereas a clear dependence was shown with respect to the surface configuration such as the minimum cross-sectional area of the specimens, the maximum depth of the pit cusp from the mean corrosion diminution level, and pitting patterns. Empirical formulae for the reduction of deformability and the reduction of energy absorption of pitted plates were proposed which may be useful in strength assessment when examining the structural integrity of aged corroded structures.

Keywords Strength · Deformability · Quasi-static load · Pitting corrosion · General corrosion · True stress–strain relationship · Mesh sensitivity · Yield ratio

1 Introduction

Marine structures are subjected to age-related deterioration such as corrosion wastage, fatigue cracking, or mechanical damage during their service life. These forms of damage can give rise to significant issues in terms of safety, health, environment, and financial costs. It is thus of great importance to develop advanced technologies that can assist proper management and control of such age-related deterioration [1]. In order to assess the structural performance of aged ships, it is of essential importance to predict the strength and absorbing energy during the collapse and/or fracture of corroded plates.

Nowadays, numerical simulation is being used to replacing time-consuming and expensive experimental work. An exact simulation of tension tests requires a complete true stress–strain relationship. Here we first estimate the true stress–strain relationship of steel plate with a rectangular cross section. A vision sensor system is employed to estimate the deformation field from the specimen surface from which an averaged least cross-sectional area and a correction factor due to the triaxial stress state can be evaluated. The measured true stress–strain relationship is then applied to an elastoplastic material model of LS-DYNA (Livermore Software Technology, Livermore, CA, USA) to assess the strength and deformability of corroded steel plates.

A great number of research projects have been carried out on the structural integrity of aged ships. Nakai et al. [2] studied the strength reduction due to periodical array of

---

Md. M. Ahmmad
Graduate School of Engineering,
Yokohama National University, 79-5 Tokiwadai,
Hodogaya-ku, Yokohama 240-8501, Japan

Y. Sumi (✉)
Faculty of Engineering, Systems Design for Ocean-Space,
Yokohama National University, 79-5 Tokiwadai,
Hodogaya-ku, Yokohama 240-8501, Japan
e-mail: sumi@ynu.ac.jp

pits, while Sumi [3] investigated the self-similarity of surface corrosion experimentally. Paik et al. [4, 5] studied the ultimate strength of pitted plates under axial compression and in-plane shear. They also derived empirical formulae for predicting the ultimate compressive strength and shear strength of pitted plates. Yamamoto [6] discussed the simulation procedure for pitting corrosion by using probabilistic models.

In the present article, we shall discuss the geometrical effect on the strength and deformability of steel plates with various pit sizes, degrees of pitting intensity, and with general corrosion. Using the probabilistic models proposed by Yamamoto and Ikegami [7], pitted surfaces of various pitting intensities were simulated and tested to obtain strength and deformability both experimentally, and numerically. The shape of pits is assumed to be conical. Empirical formulae are proposed to estimate the reductions in deformability and energy absorption capacity, and these were verified by experimental and numerical results. In the case of general corrosion, replica specimens were made to simulate corroded surfaces sampled from an aged heavy oil carrier. In experiments, the geometries of corroded surfaces were generated by a computer-aided design (CAD) system and were mechanically processed by a numerically controlled (NC) milling machine in a computer-aided manufacturing (CAM) system. Investigations were made for two different steels with the same ultimate strength, but having yield ratios of 0.657 (steel A) and 0.841 (steel B), to identify the material effects of corrosion damage. Note that the former type of steel is commonly used for marine structures.

2 Measurement of true stress–strain relationship

The true stress–strain relationship, including the material response in both pre- and postplastic localization phases, is necessary as input for numerical analyses. In some cases, structural analysts use a power law stress–strain relationship. It has been demonstrated that power law stress–strain curves for certain steels may overestimate the actual stress–strain curve at low plastic strain, while underestimating it in the later stages [8]. For thick sections, the true stress–strain relationship can conveniently be determined by using a round tensile bar, while for thin sections it is better to use specimens with a rectangular cross section [9]. However, strain measurement becomes complicated, especially for flat tensile specimens, due to the inhomogeneous strain field and triaxial stress state. Two practical difficulties can be mentioned here. The first problem is the measurement of the instantaneous area of minimum cross section after necking. During plastic instability, the cross section at the largest deformed zone forms a cushion-like shape [10], so that it is difficult to measure the cross-sectional area at the neck. The second challenge is the measurement of a/R, where a is the half-thickness and R is the radius of curvature of the surface at the neck (see Fig. 1), to estimate a correction factor, e.g., Bridgman [11] and Ostsemin [12] correction factors for the triaxial stress condition after necking.

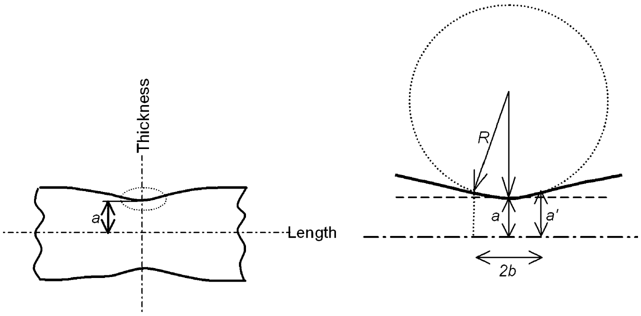

Fig. 1 Illustration of necked geometry. *a* half-thickness of the neck, *a′* half-thickness at location b, *R* radius of curvature of the surface at the neck

2.1 True stress and true strain

For any stage of deformation, true stress and true strain are defined by:

$$\sigma_T = \frac{F}{A}, \quad \varepsilon_T = \ln\left(\frac{l}{l_0}\right) \tag{1}$$

where A, F, l_0, and l are the instantaneous area, the applied force, the initial length of a very small gauge length (say 1 mm) at the possible necking zone, and its deformed length, respectively. As long as uniform deformation occurs, the true stress and strain can be calculated in terms of engineering stress, σ_e, and engineering strain, ε_e, by:

$$\varepsilon_T = \ln(1 + \varepsilon_e); \quad \sigma_T = \sigma_e(1 + \varepsilon_e) \tag{2}$$

The effective strain, $\bar{\varepsilon}$, after bifurcation was calculated by Scheider et al. [10] as:

$$\bar{\varepsilon} = \sqrt{\frac{4}{3}(\varepsilon_I^2 + \varepsilon_I\varepsilon_{II} + \varepsilon_{II}^2)} \tag{3}$$

where ε_I and ε_{II} are the true strains in the specimen's length and width directions, respectively. Usually bifurcation phenomena occur soon after the maximum load. In our calculations, we shall use Eq. 3 to measure the true strain.

After the initiation of necking, true stress can be calculated by:

$$\sigma_T = \frac{F}{A} = \frac{F}{A_0}\exp(-\varepsilon_{II} - \varepsilon_{III}) \tag{4}$$

where ε_{III} is the strain in the thickness direction. In the case of uniform deformation, Eq. 4 can be calculated as:

$$\sigma_T = \frac{F}{A_0}\exp(\varepsilon_I) \tag{5}$$

In practice, the axial strain over the cross section, as shown in Fig. 2a, is not uniform, so that an average true stress can be obtained from Eq. 6 by measuring an average axial strain, $\bar{\varepsilon}_I$ (see Fig. 2b):

$$\sigma_T = \frac{F}{A_0}\exp(\bar{\varepsilon}_I) \tag{6}$$

The true equivalent stress after the correction due to the triaxial stress state can be expressed as:

$$\sigma_{eq} = \frac{\sigma_T}{C_B} \quad \text{or} \quad \frac{\sigma_T}{C_O} \tag{7}$$

where C_B and C_O are two analytical correction factors that can be used for rectangular cross-section specimens after the initiation of necking. These factors are given by Bridgman [11]:

$$C_B = \left[\left(1+\frac{2R}{a}\right)^{1/2} \ln\left\{1+\frac{a}{R}+\left(\frac{2a}{R}\right)^{1/2}\left(1+\frac{a}{2R}\right)^{1/2}\right\}-1\right] \tag{8}$$

and by Ostsemin [12]:

$$C_O = \left(1+\frac{a}{5R}\right) \tag{9}$$

where a and R are defined as illustrated in Fig. 1, in which the solid bold line represents the upper surface of the centerline section of the neck. The correction factors C_B and C_O depend on a parameter, a/R, given by:

$$\frac{a}{R} = \frac{2a(a'-a)}{(a'-a)^2+b^2} \tag{10}$$

where a/b may be taken as 0.5–1.0 [13], and the half thickness, a', is estimated at a distance b from the center of the neck (see Fig. 1). The continuous values of the thickness can be estimated by the surface strains in the length and width directions by the vision sensor by applying the following relations:

$$a = a_0\exp(\varepsilon_{III}) = a_0\exp(-\varepsilon_I - \varepsilon_{II}) \tag{11}$$

$$a' = a_0\exp(\varepsilon'_{III}) = a_0\exp(-\varepsilon'_I - \varepsilon'_{II}). \tag{12}$$

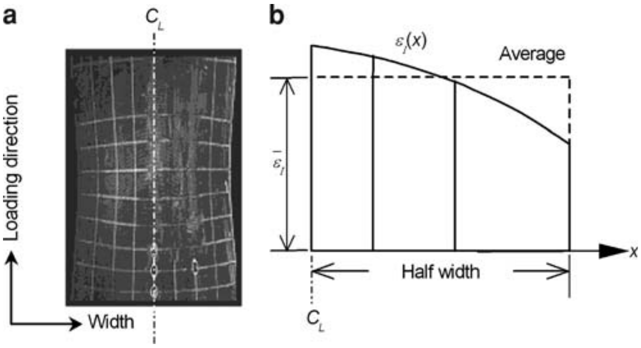

Fig. 2 **a** Deformed grid on the surface of necked zone. **b** Estimation of average axial strain ($\bar{\varepsilon}_I$). C_L center line

2.2 Experimental procedures

The geometry of the flat specimen is shown in Fig. 3a. The specimen surface is prepared as shown in Fig. 3b: white dots on permanent black ink are painted on the specimen. The relatively long length, 40 mm, of the measuring zone is designed so that necking occurs within this range without introducing any imperfections to the test specimen.

Figure 4 shows the experimental setup. The monochromic vision sensor traces the white dots during the experiment. Since the white paint should have high deformability to follow the large deformation, we use correction fluid for the white dots. An extensometer is also used to measure the strain of gauge length 100 mm. Having read the position of the dots on the specimen surface, these digital data are converted to analog data by a D/A converter, where the deformation data and load data are synchronized on a personal computer through a voltage signal interface. A programmable logical controller is used to synchronize the whole system.

2.3 Test results

In this study we observe that uniform deformation occurs until the first bifurcation (initiation of diffuse neck) at strain 0.25, and the strain at maximum load is 0.16 for steel A. The correction factor due to the triaxial stress state becomes effective after the second bifurcation at strain

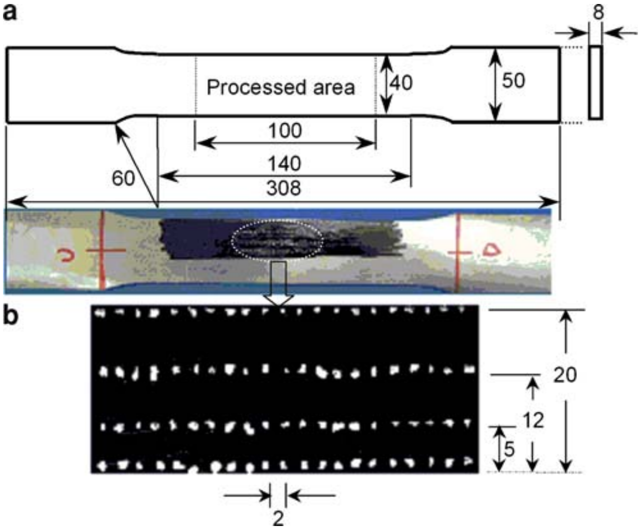

Fig. 3 **a** The tensile specimen (all dimensions in mm). **b** *White dots* are added to the specimen and are used by the vision sensor system

0.45. The correction factor varies from 1 to 1.03, which implies that the true stress is reduced by 0–3% after the second bifurcation. Applying the procedure discussed in the previous subsection, the true stress–strain relationships are obtained for steel A and steel B as illustrated in Fig. 5a and b. Note that the true stress–strain relationships with the Ostsemin correction factor are used for the finite element analyses in the subsequent sections.

3 Numerical analysis

Numerical analyses were carried out by using a nonlinear implicit finite element code, LS-DYNA, as the problem is a quasi-static type. The constitutive material model is an elastoplastic material where an arbitrary stress versus strain curve can be defined. This material model is based on the J_2 flow theory with isotropic hardening [14].

3.1 Finite element model and material properties

The basic problem that was analyzed is the quasi-static uniaxial extension of a rectangular bar, as shown in Fig. 6. Due to the symmetry, only one octant of the specimen is analyzed using the finite model discretized by 8-node brick elements as shown in Fig. 6b. A constant velocity, $V(t)$, of 3 mm/min is prescribed in the x direction. The material properties are listed in Table 1, and the strain hardening is defined by the true stress–strain curves illustrated in Fig. 5a and b. The fracture strain, ε_f, is measured by:

$$\varepsilon_f = \ln\left(\frac{A_0}{A_f}\right) \tag{13}$$

where A_f is the projected fracture surface area measured after the experiments.

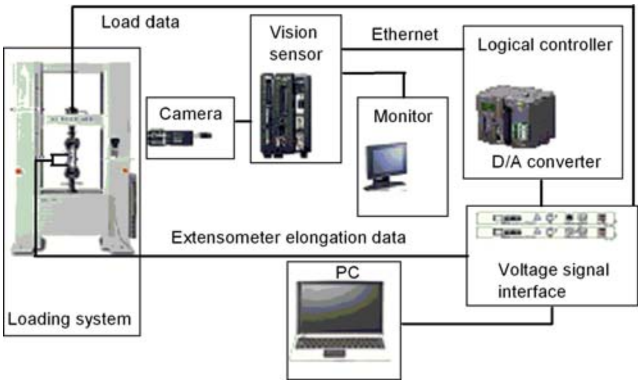

Fig. 4 Experimental setup and vision system. *D/A* digital to analog

3.2 The effect of mesh size

Mesh size effects are crucial in the failure analyses of structures. In general, a finer mesh size is needed for accurate results when large deformation accompanies strain localization. However, a significant complication arises because of mesh size sensitivity whereby the strain to failure increases on refining the mesh. The failure strain of the finite element analyses is defined as the maximum plastic strain, i.e., when the nominal strain reaches 0.284 (steel A), at which the flat specimen failed in the experiments. In Fig. 7, we compare the failure strains of five finite element models at the same nominal strain at failure. In these cases, we only change the element size, h_x, in the loading direction, keeping the mesh size constant at 1 mm in the remaining two directions, h_y and h_z, because their effect is not so significant. From the figure, it can be seen that the finer the mesh size the higher the maximum plastic strain. Figure 8 represents a comparison of experimental and numerical nominal stress–strain relationships for a flat plate of steel A. The element size is 0.5 × 1 × 2 (mm). Similar results were obtained for steel B, for which the numerical results agree well with the experimental values.

4 Pitting corrosion and its effect

Pitting is an extremely localized form of corrosion. It typically occurs in the bottom plating of oil tankers, in structural details that trap water, and in the hold frames of cargo

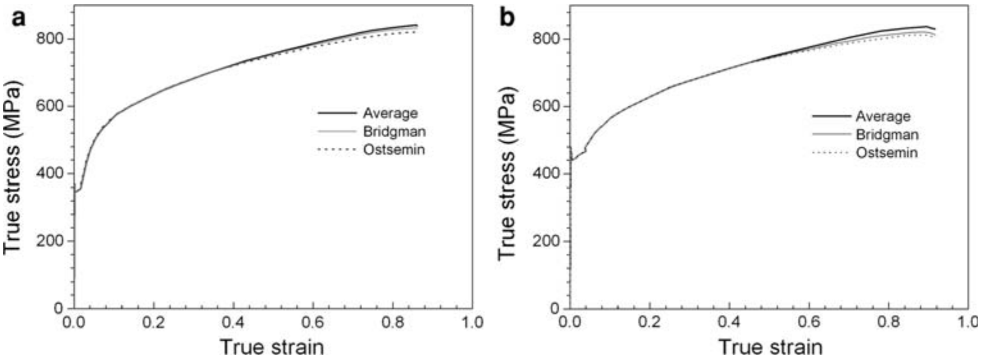

Fig. 5 True stress–strain relationship of **a** steel A and **b** steel B; average true stress defined by Eq. 6, and the corrected equivalent stresses defined by Eq. 7

holds of bulk carriers that carry coal and iron ore. When the effect of corrosion on local strength and deformability is considered, pitting corrosion is of great concern. The effect of pitting corrosion on the compressive and shear strengths has been studied both experimentally and numerically by several researchers. In the present study, we shall investigate in detail the tensile strength, focusing attention on the deformability and energy absorption capacity.

4.1 Simulation of plates with a single pit and periodical arrays of pits

In this subsection, we shall discuss the simulation procedure of steel plates with a single pit or a periodical array of pits. In addition, we shall observe the effect of pit size on the nominal stress–strain relationship of plates with a single pit. To estimate the effect of pit size on strength and deformability, we consider three different pit sizes (diameters of 10, 20, and 40 mm) whose depth-to-diameter ratio is 1:8.

At first, the true stress–strain relationships of steels A and B will be applied to specimens with surface pit configurations as specified in Table 2. Figure 9a and b show the specimens and mesh pattern of the one quadrant of the model, respectively. The mesh sensitivity within the pit cusp was analyzed by changing the mesh size along the thickness direction, while those in the other directions remained constant; the radial mesh size and the circumferential mesh angle were 0.5 mm and 4.5°, respectively. By refining the mesh size within the pit cusp, the maximum plastic strain in the longitudinal direction calculated at nominal failure strain, 0.175, sharply increased, as shown in Fig. 10. The experimental and numerical results of the nominal stress–strain relationship of steel A are shown in Fig. 11a and b, respectively, in which we can observe good agreement. Similar results were also obtained for steel B.

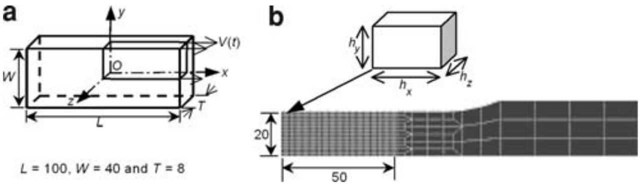

Fig. 6 Finite element model of a flat specimen. **a** the one-eighth analyzed, **b** mesh and element pattern

Nakai et al. [2] and Sumi [3] have experimentally investigated the strength and deformability of steel plates with periodical arrays of surface pits (see Fig. 12a–d). Periodical pits were made on both surfaces of a plate and they were arranged asymmetrically with respect to the middle plane of the specimen (see Fig. 12e). To make a finite element model, we first generated an array of points that describes the surfaces with these pits. From this point data we can obtain a nonuniform rational B-spline (NURBS) surface [15] that can be discretized using isomesh. Having obtained the data for the front and back surfaces, solid elements (8-node hexahedrons) can be generated by a sweeping action, as shown in Fig. 12f. The

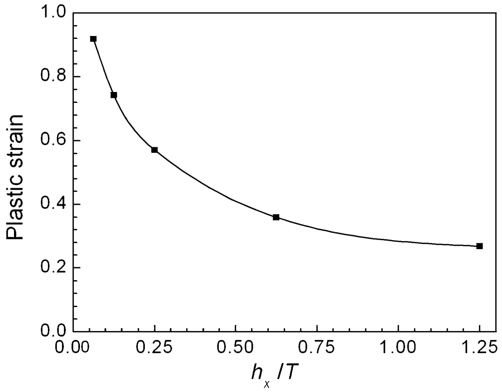

Fig. 7 Effect of mesh size on maximum plastic strain at failure (steel A). h_x length of each element, T sample thickness

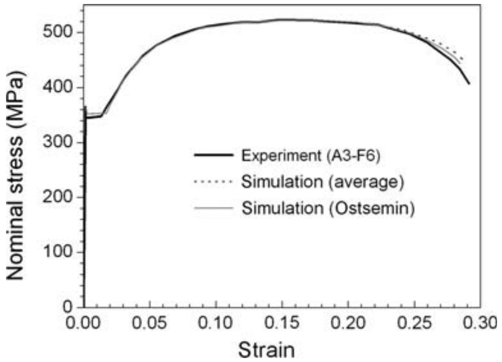

Fig. 8 Verification of numerical nominal stress–strain relationship by experimental results (steel A)

Table 1 Material properties

Material	Yield strength (N/mm^2)	Tensile strength (N/mm^2)	Y/T ratio	E (GPa)	Poisson's ratio	Elongation (%)	Failure strain
Steel A	344	523	0.657	206.5	0.3	28.41	0.92
Steel B	440	523	0.841	204.5	0.3	28.94	0.90
SM490A	325	513	0.634	206	0.3	32.46	

Y/T yield strength to tensile strength ratio, *E* Young's modulus

Table 2 List of tensile test specimens of flat plate and plate with a single pit or a periodical array of pits

No.	Material	No. of pits		Pit diameter (mm)
		Side 1	Side 2	
A3-F3	A	0	0	0
A3-F6	A	0	0	0
A3-F8	A	0	0	0
A3-10	A	1	0	10
A3-20	A	1	0	20
A3-40	A	1	0	40
A3-20-8 (1)	A	8	8	20
A3-20-8 (2)	A	8	8	20
B3-F1	B	0	0	0
B3-10	B	1	0	10
B3-20	B	1	0	20
B3-40	B	1	0	40
B3-20-8 (1)	B	8	8	20
B3-20-8 (2)	B	8	8	20
SM490A-20-2[a]	SM490A	2	0	20
SM490A-20-4[a]	SM490A	4	4	20
SM490A-20-4[a]	SM490A	6	6	20
SM490A-20-8[a]	SM490A	8	8	20

All specimen dimensions are as shown in Fig. 3a

The diameter to depth ratio of all pits is 8:1

[a] From Sumi [3]

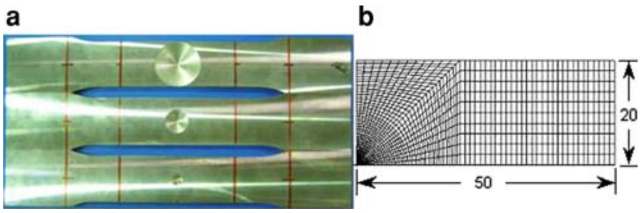

Fig. 9 Pitting surfaces: **a** specimens with a single pit, **b** mesh pattern of the quadrant of the processed zone (50 × 20 × 8 mm)

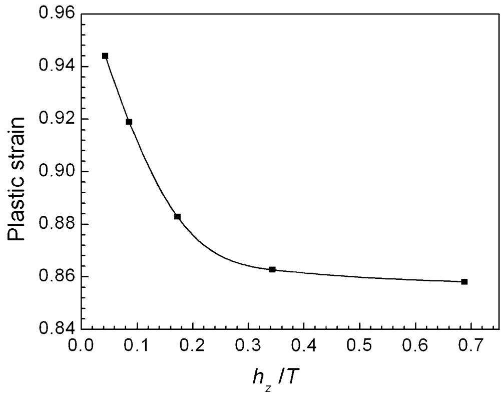

Fig. 10 Mesh size sensitivity on plastic strain in the loading direction at the pit cusp (steel A)

numerical and experimental nominal stress–strain curves of steels A and B are shown in Fig. 13. Here the failure strain is defined as 0.7, as the element size is 1 × 1 × 4 mm. A good agreement is observed among experimental and numerical nominal stress–strain curves until the strain reaches about 0.15 (see Fig. 13).

4.2 Validation of numerical results

Nakai et al. [2] and Paik et al. [4] have confirmed that the ultimate strength of a steel plate with pitting corrosion is governed by the smallest cross-sectional area. Here we also consider the ultimate strength reduction factor, R_u, as a function of damage. The damage value depends on the smallest cross-sectional area, A_p, due to surface pits and can be defined as:

$$\text{Damage, } D_m = \frac{A_0 - A_p}{A_0} \tag{14}$$

where A_0 is the intact sectional area, and R_u is defined as:

$$R_u = \frac{\sigma_{up}}{\sigma_{u0}} \tag{15}$$

where σ_{u0} and σ_{up} are the ultimate tensile strength of intact plates and pitted plates, respectively. Figure 14 shows that the strength reduction factor decreases with increasing damage of steels A and B. Sumi [3] experimentally investigated the strength and deformability of artificially pitted plates of SM490A steel with a yield ratio 0.63, whose results as well as the present numerical results are presented in this section (see Figs. 14, 15, 16). Note that the damage value of all models with periodical array of surfaces pits is 0.15625. In Fig. 14, R_u, slightly decreases with the increase of pit number for periodical pits.

We define the reduction of deformability, R_d, due to surface pits as:

$$R_d = \frac{e_p}{e_0} \tag{16}$$

where e_0 and e_p are the total elongation of flat and pitted specimens, respectively, under uniaxial tension. Figure 15 shows the reduction of deformability, R_d, as a function of damage of plates with a single pit and a periodical array of pits obtained by experiments and simulations. It is observed in single-pit problems that the deformability decreases with increasing damage, while in periodical-pit problems it increases with the total number of pits.

Let us introduce another parameter—the reduction of energy absorption, R_e, as:

$$R_e = \frac{E_p}{E_0} \tag{17}$$

where E_0 and E_p are the total energy absorbed by an intact flat plate and a pitted plate, respectively, in uniaxial

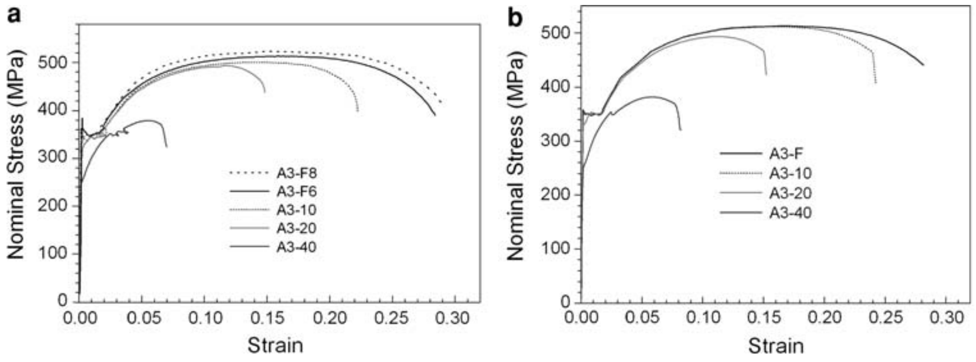

Fig. 11 Nominal stress–strain curves for various single-pit specimens made of steel A. **a** Experimental values, **b** calculated values

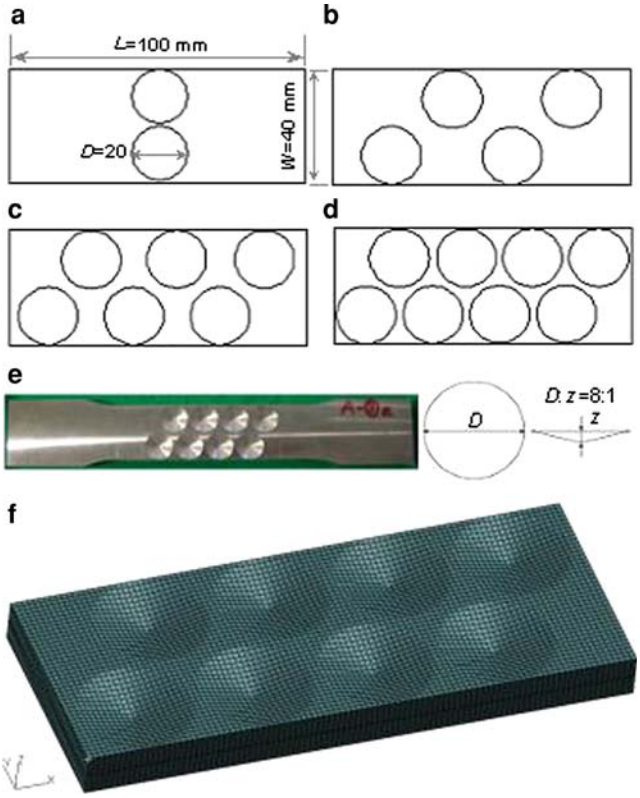

Fig. 12 Periodical array of pits; **a** pits on one side, **b–d** pits arranged asymmetrically on both sides, **e** test specimen with periodical pits and pit geometry, and **f** mesh pattern of pitted model

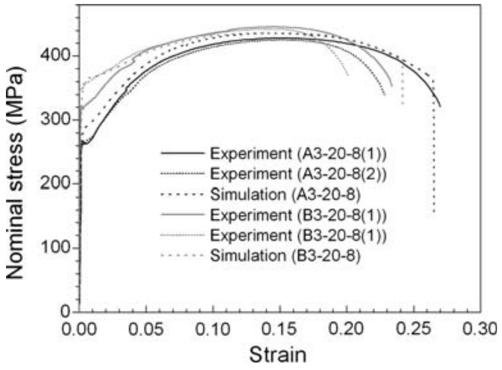

Fig. 13 Verification of numerical stress–strain relationships using experimental data for plates with periodical array of surface pits

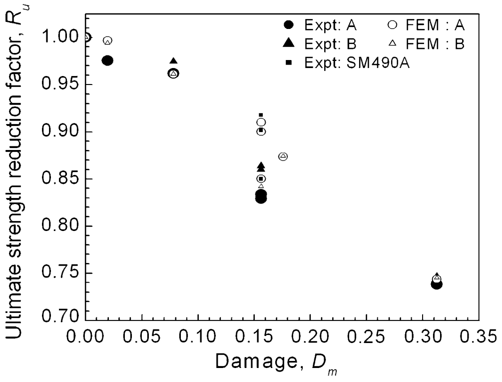

Fig. 14 Strength reduction due to damage caused by a single pit and a periodical array of pits. *A* and *B* represent steels A and B, respectively, and SM490 was the steel type used by Sumi [3], whose results are used here. *FEM* finite element method

tension. The energy can be measured by integrating the area under the nominal stress–strain curves. Figure 16 shows the reduction of energy absorption, R_e, as a function of damage, D_m, for various pitted plates. Here, also, R_e decreases with the increase in damage value in single-pit problems, and it increases with the increase in the number of pits in periodical-pit problems.

From Figs. 14, 15, 16, it can easily be seen that the deformability and energy absorption capacity reduce considerably with increasing pit size, while the strength reduces moderately. Also, we can observe that the differences in the reduction of the strength, deformability, and energy absorbing capacity of steels A and B are insignificant. In general, we observed a good agreement between the numerical and experimental results for the pit problems.

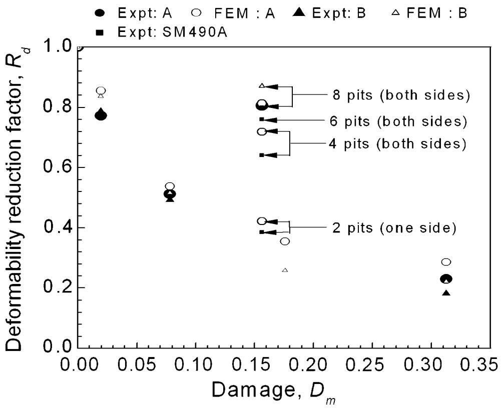

Fig. 15 The reduction of deformability, R_d, as a function of damage for plates with a single pit and periodical pits under uniaxial tension. The samples had one pit unless otherwise stated

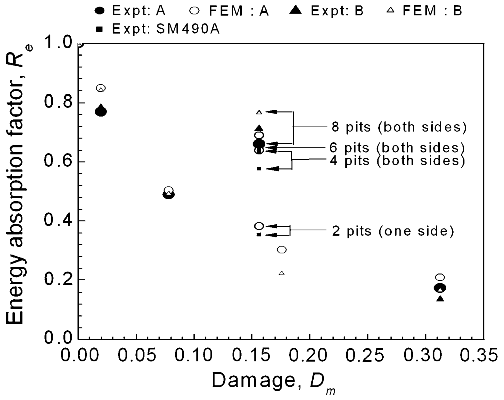

Fig. 16 The reduction of energy absorption, R_e, as a function of damage for plates with a single pit and a periodical array of pits under uniaxial tension. The sample had one pit unless otherwise stated

5 Simulation of plates with random arrays of pits

Yamamoto and Ikegami [7] discussed the mathematical models by which the surface condition of structural members with corrosion pits can be generated. According to their probabilistic models, the generation and progress of corrosion involves the following three sequential processes: the generation of active pitting points, the generation of progressive pitting points, and the progress of pitting points. The life of a paint coating can be assumed to follow a lognormal distribution given by:

$$f_{T_0}(t) = \frac{1}{\sqrt{2\pi}\sigma_0 t} \exp\left\{-\frac{(\ln t - \mu_0)^2}{2\sigma_0^2}\right\} \tag{18}$$

where T_0 is the life of the paint coating and μ_0 and σ_0 are the mean and standard deviation of $\ln(T_0)$. Active pitting points are generated after time, T_0. The transition time, T_r, from active pitting points to progressive pitting points is assumed to follow an exponential distribution:

$$g_{T_r}(t) = \alpha \exp(-\alpha t) \tag{19}$$

where α is the inverse of the mean transition time. The progress behavior of pitting points after generation is expressed as:

$$z(\tau) = c\tau^{\beta} \tag{20}$$

where τ is the time elapsed after the generation of progressive pitting points with the coefficients c and β. Coefficient c is determined as a lognormal distribution:

$$h_c(c) = \frac{1}{\sqrt{2\pi}\sigma_c c} \exp\left\{-\frac{(\ln c - \mu_c)^2}{2\sigma_c^2}\right\} \tag{21}$$

where μ_c and σ_c are the mean and standard deviation of $\ln(c)$. The value of coefficient β is considered to vary from 1 to 1/3, depending on the materials and the corrosive environment.

In this study, the shape of the corrosion pit is defined by the following shape function:

$$S(\mathbf{x} - \mathbf{x_0}, D_0, \chi_0) = 2\chi_0\left(\max\left\{0,\ \frac{D_0}{2} - \sqrt{(x_0 - x)^2 + (y_0 - y)^2}\right\}\right) \tag{22}$$

where:

$$\chi_0 = \frac{z_0}{D_0}, \quad \mathbf{x_0} = (x_0,\ y_0), \quad \mathbf{x} = (x,\ y)$$

The position vectors of the pit center and that of an arbitrary surface point are denoted by $\mathbf{x_0}$ and $\mathbf{x}$, respectively. The depth and diameter of a corrosion pit at $\mathbf{x_0}$ are represented by z_0 and D_0. The ratio of the diameter to the depth of the pits was observed to vary from 6 to 10. It is assumed that χ_0 is a random variable that follows a normal distribution given by:

$$f_\chi(x) = \frac{1}{\sqrt{2\pi}\sigma_\chi} \exp\left\{-\frac{(x - \mu_\chi)^2}{2\sigma_\chi^2}\right\} \tag{23}$$

where $\mu_\chi = 0.125$ and $\sigma_\chi = 0.015625$ [6].

We shall consider a plate taken from a hold frame of a bulk carrier with dimensions of 200 × 80 × 16 mm. Having generated various stochastic pitting patterns due to corrosion, we shall simulate the resulting strength and deformability. The numerically generated corroded surface depends considerably on the number of possible pitting points on the surface. We assume that the maximum density of pitting initiation points is, approximately, 1 pit/53 mm^2. The assumed parameters of the probabilistic models are given in Table 3.

Table 3 Parameters of probabilistic models [7]

	μ_0	σ_0	$1/\alpha$	$1/\beta$	μ_c	σ_c
Bulkhead (cargo hold)	1.701	0.68	1.90	2.0	0.0374	0.3853

μ_0, σ_0, mean and standard deviation of $\ln(T_0)$; α, β, parameters defined by Eqs. 19 and 20; μ_c, σ_c, mean and standard deviation of $\ln(c)$ in Eq. 21

5.1 Statistics of the corrosion condition

Once we obtain the probabilistic parameters, we can simulate the corroded surface by using the shape function given by Eq. 22. Let us discuss some statistical characteristics of pitting corrosion. Average corrosion diminution is defined as the average thickness loss due to corrosion in each year. If $z(\mathbf{x})$ denotes the depth of corrosion at any point $\mathbf{x}(x, y)$ on the surface, we can obtain the average corrosion diminution, z_{avg}, by:

$$z_{\text{avg}} = E[z(x,y)] = \frac{1}{MN}\sum_{m=1}^{M}\sum_{n=1}^{N} z(x_m, y_n) \tag{24}$$

where M and N are the number of sections in the x and y directions. In general, Eq. 24 can be evaluated from discrete point data. Figure 17 shows the thickness diminution of five sampled plates over 20 years obtained from the same probabilistic parameters as those listed in Table 3. Thickness diminution progresses linearly after the failure of the coating protection system (CPS). In this case, thickness diminution starts after approximately 5 years.

The degree of pitting intensity (DOP) is defined as the ratio of the pitted surface area to the whole surface area. According to the unified rules of the International Association of Classification Societies (IACS), if the DOP in an area where coating is required is higher than 15%, then thickness measurement is required to check the extent of corrosion. Figure 17 shows the increase in the degree of pitting intensity with a structure's increasing age. During the first 2.5–10 years, DOP increases rapidly because of the quick deterioration of the protective coating system.

We shall investigate the strength and deformability of these five sampled plates at various corrosion stages. For finite element simulations, we intend to select six characteristic points from each sample. The various characteristics of numerical calculations and experiments are shown in Table 4. We carried out four experiments for the possible validation of the corresponding finite element results.

5.2 Simulated corrosion surfaces based on a probabilistic model

In order to simulate the strength and deformability of corroded plate, a question may arise as to how the results may change with the plate width. This problem has been discussed by Nakai et al. [2] by using small and wide specimens, where the width and gauge length were 80 and 200 mm for small specimens and 240 and 400 mm for wide specimens. Although there is some scatter in their experimental data, the strength reduction can basically be estimated in both cases by using the area of minimum cross section, A_p, perpendicular to the loading axis. On the other hand, deformability obviously depends on the definition of the gauge length of the plate. They also observed the same level of deformability in a small specimen as that in a wide plate when the elongation of a wide plate was measured in a similar gauge length along the fracture zone. From these observations, we decided to simulate the mechanical behavior of an area of 200 × 80 mm in the following analyses.

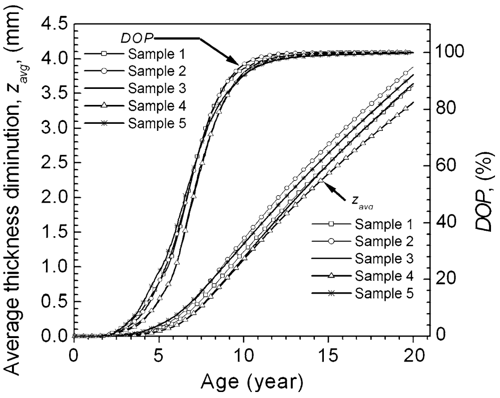

Fig. 17 Average thickness diminutions (z_{avg}) and degrees of pitting intensity (*DOP*) versus the age of the structure for five sampled plates (200 × 80 × 16 mm)

The surface corrosion conditions of the corroded area are simulated for six different DOPs from each sample. Figure 18a–f show the simulated corrosion conditions of sample 1. Figure 19 shows the test specimens with 19, 51, 92, and 100% DOP (sample 1). Note that the sizes of the processed area of the test specimens are self-similar with a scale factor of 0.5 with respect to the original size. According to Sumi [3], a self-similar specimen behaves similarly within this scaling factor if the same quantity of geometrical information is contained in both models.

The procedure of surface processing of test specimens is briefly explained. We first make an array of points that describe the corroded surface based on probabilistic corrosion models. From this data we obtained a NURBS surface generated by CAD software Rhinoceros (McNeel, Seattle, WA, USA). The generated surface was imported into CAM software Mastercam (CNC, Tolland, CT, USA) to process the specimen surfaces for the experiments, and it was also imported into Patran (MSC, Santa Ana, CA, USA) for the finite element analyses. The top and the bottom

Table 4 Characteristics of the simulated plates and test specimens with random pits

No.	Age (year)	DOP (%)	z_{avg} (mm)	Damage, D_m	P_{max} (mm)
Sample 1					
1[a]	5.0	18.99	0.055	0.024	1.444
2[a]	6.75	51.2	0.173	0.044	1.822
3	7.75	73.24	0.296	0.0693	2.006
4[a]	9.5	92.37	0.54	0.114	2.779
5	13.0	99.11	1.002	0.189	2.293
6[a]	17.0	99.99	1.48	0.2626	3.501
Sample 2					
7	5.0	19.23	0.0621	0.025	1.475
8	6.7	50.36	0.207	0.073	1.994
9	7.85	74.96	0.367	0.11	2.354
10	9.3	91.79	0.593	0.156	2.753
11	13.5	99.868	1.194	0.26	3.64
12	19.0	100.0	1.836	0.367	4.55
Sample 3					
13	3.7	15.09	0.0116	0.012	1.11
14	6.15	45.2	0.0871	0.034	1.584
15	7.5	69.8	0.222	0.055	1.79
16	9.5	89.9	0.495	0.098	2.06
17	12.0	98.4	0.849	0.16	2.78
18	18.0	100.0	1.597	0.275	4.05
Sample 4					
19	4.7	10.23	0.027	0.018	1.294
20	6.65	40.05	0.127	0.044	1.732
21	7.5	59.73	0.216	0.0608	1.891
22	9.5	89.09	0.483	0.103	2.221
23	13.5	98.88	1.00	0.1776	2.76
24	20.0	99.95	1.685	0.2771	3.74
Sample 5					
25	4.1	12.59	0.0372	0.034	1.332
26	5.85	35.03	0.1398	0.064	1.84
27	6.85	55.28	0.2417	0.082	2.075
28	8.4	80.18	0.4447	0.112	2.394
29	11.0	95.47	0.805	0.1575	2.85
30	17.5	99.43	1.61	0.256	3.75

DOP degree of pitting, z_{avg} average thickness diminution (Eq. 24), D_m damage, P_{max} maximum depth of pit

[a] Test with steel A

surfaces as well as the internal surface of the specimen are generated so that they are discretized by isomesh. The three-dimensional solid finite element model was obtained by the same procedure discussed in Sect. 4.1. It consists of 16720 8-node solid elements with a minimum size in the processed area of 0.5 × 1 × 1 mm. We control the minimum element size in the thickness direction by defining a two-layered model with an internal surface 1 mm below the cusp of the deepest pit.

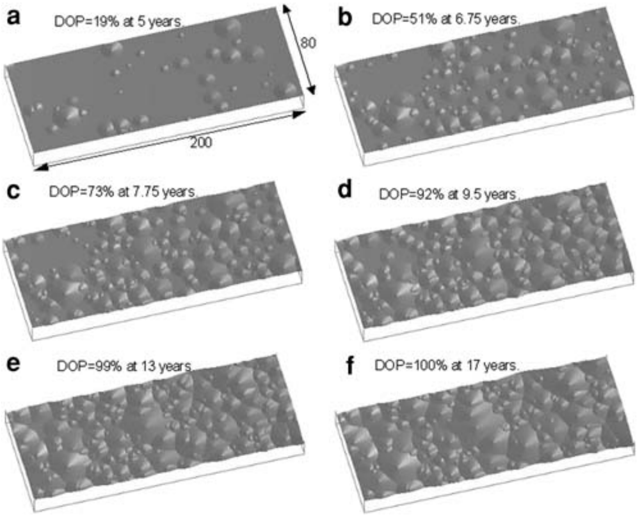

Fig. 18 Simulated pitting corrosion surfaces (sample 1)

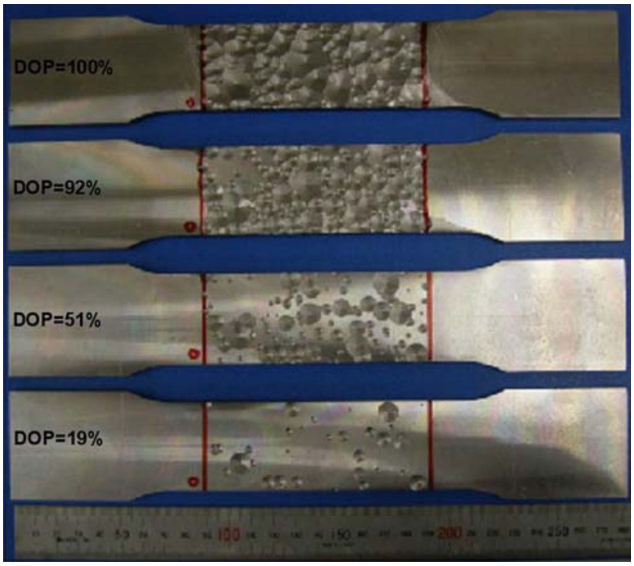

Fig. 19 Test specimens (100 × 40 × 8 mm) with 19, 51, 92, and 100% DOP (sample 1)

The accuracy of the geometries of the test specimens and finite element models were confirmed by comparing them with the original data of the probabilistic corrosion model. Figure 20 compares the various thickness distributions of the finite element models and the test specimens along their length. These are obtained by:

$$E[z_W(x)] = \frac{1}{W} \int_{-W/2}^{W/2} z(x,y)\mathrm{d}y \tag{25}$$

where W is the width of the corroded plate, and $z(x, y)$ is the corrosion diminution at point (x, y) on the surface. The finite element data coincides with the original data. Having used a cutting tool of 2-mm diameter for processing the test specimens, a slight difference is observed with the original data as shown in the figure.

5.3 Results and discussions

Figure 21a, b show the nominal stress–strain curves of steel A obtained by simulations and experiments (sample 1). Generally speaking, strength and deformability decrease with increasing DOP. If we compare the numerical and experimental results, we can see that the experimental results give approximately 3% higher strength values than those generated by the numerical calculations. Of course, we observe a slight variation of strength and deformability in different tests of the same material ($Y/T = 0.657$). Note that all finite element analyses with steel A were carried out for a constant ultimate strength of 513 MPa.

Figure 22a–d show comparisons of the location of failure in simulations and experiments for four different corrosion conditions (sample 1). In the numerical simulations, considering the mesh size sensitivity shown in Fig. 7, element failure is assumed when the strain of an element reaches 0.92, and the corresponding element stiffness is set to zero afterwards. The location of maximum pit depth, the minimum cross-sectional area, and the location of failure in numerical and experimental specimens are listed in Table 5 for sample 1. For numerical models with their DOPs of 19, 92, 99, and 100%, failure occurs at or near the minimum cross-sectional area, while for DOP 51 and 73% it occurs along the favorable shear band formed prior to the failure. We can see that the simulated failure locations certainly coincide with their experimental counterparts.

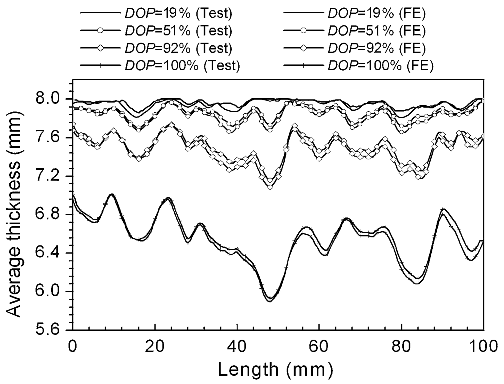

Fig. 20 Accuracy check for test specimens and finite element (*FE*) models (sample 1)

To understand the cause of failure, we have monitored the whole process of plastic deformation in simulations as well as in experiments. We observe that stress concentration occurs at each pit cusp during the entire loading process. After the maximum load, unloading starts from both ends of the specimen. A shear band forms at a favorable direction in relation to the pit orientation, which leads to failure initiation from the minimum thickness on the shear band.

In Sect. 4.2 we discussed the strength reduction factor for plates with a single pit and a periodical array of pits as a function of damage, which is estimated based on the smallest cross-sectional area. In the case of the probabilistic corrosion model, the total number of pits as well as the damage increases with time. Figure 23 shows the experimental and numerical results of ultimate strength reduction with increasing damage due to pitting corrosion for all pitted models of steels A and SM490A. The strength reduces approximately 20% within 20 years. It was confirmed that the tensile strength of pitted plates can be predicted by the empirical formula proposed by Paik et al. [4] for the compressive strength of pitted plates:

$$R_u = (1 - D_m)^{0.73} \tag{26}$$

How much does deformability reduce with the progress of corrosion? Which parameters does it depend on? We have investigated the answers of these questions. We found that deformability does not have a good correlation with the maximum pit depth (P_{max}) or with damage (D_m), directly. Rather, it has a very good correlation with surface roughness, characterized by the quantity R_p or R_s, defined by:

Fig. 21 Numerical and experimental nominal stress–strain curves of plates with random pits (sample 1, steel A): **a** simulation results, **b** experimental results

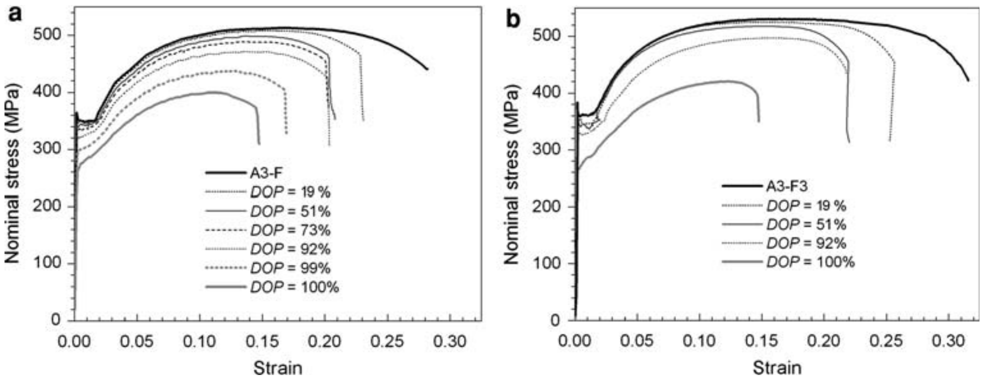

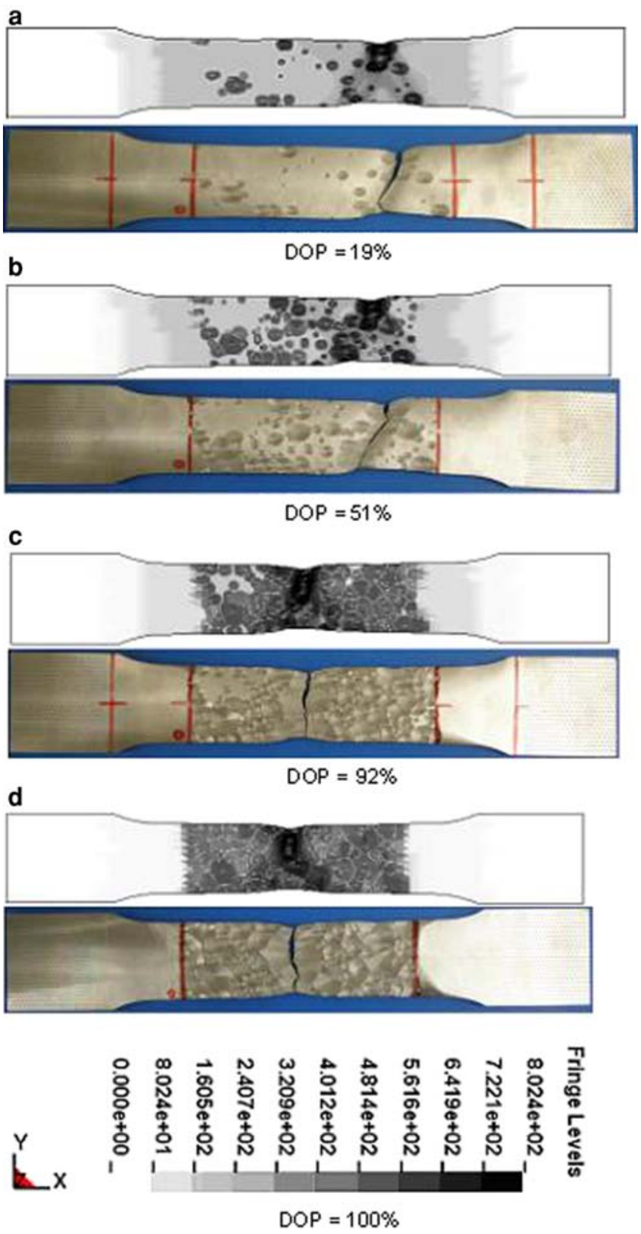

Fig. 22 Locations of failure for different DOP values in simulation (*upper*) and experiment (*lower*) with von Mises stress distribution at failure (steel A, sample 1)

$$R_p = \frac{P_{max} - z_{avg}}{T} \tag{27}$$

or

$$R_s = D_m - \frac{z_{avg}}{T} \tag{28}$$

where T is the thickness of the intact plate. The maximum surface roughness, R_p, is the relative difference between the depth of the deepest pit, P_{max}, and the average corrosion diminution, z_{avg}. On the other hand, the parameter R_s is the relative difference between the average thickness at the section of the minimum cross-sectional area and the average corrosion diminution, z_{avg}.

Figure 24 shows the reduction of deformability, R_d, (Eq. 16) of all the pitted models of steel A and SM490A discussed earlier as a function of maximum surface roughness, R_p. Based on the simulation results of randomly distributed pits, the following empirical formula can be derived by regression analysis to predict the deformability:

$$R_d = 1 - 0.2R_p - 5.3R_p^2, \quad \text{for } 0 \le R_p \le 0.35 \tag{29}$$

As shown in Fig. 24, the experimental results of specimens with a single pit, a periodical array of pits, and randomly distributed pits fall closely to the values given by Eq. 29 in the range $0.0 \le R_p \le 0.35$.

Figure 25 shows the reduction of deformability as a function of surface roughness based on R_s values. Similarly, based on the simulation results of randomly distributed pits, the following empirical formula can be derived to predict the deformability:

$$R_d = 1 - 8.14R_s + 26.4R_s^2, \quad \text{for } 0 \le R_s \le 0.15 \tag{30}$$

As shown in Fig. 25, the experimental and numerical results of specimens with a single pit and with randomly distributed pits fall closely to the values given by Eq. 30 in the range $0.0 \le R_s \le 0.15$, while some deviations exist for specimens with periodical pits.

The relationship of the reduction of energy absorption, R_e, in terms of R_u and R_d is illustrated in the three-dimensional plot of Fig. 26. The value of R_e can be approximated by the following empirical formula:

$$R_e(D_m, R_p \text{ or } R_s) \equiv R_u(D_m)R_d(R_p \text{ or } R_s) \tag{31}$$

the surface of which is also illustrated in Fig. 26. The validity of the above equation is examined in Fig. 27 by applying Eqs. 15–17 to the experimental and simulated data; a good correlation results. The simple predictions of the reduction of energy absorption, R_e, by Eq. 31 with the use of R_u from Eq. 26 and R_d from Eqs. 29 or 30 are also examined in the same figure by comparing with the simulated and experimental results. The correlation is again very satisfactory.

In order to estimate the reduction of strength, deformability, and energy absorption, it is essential to know the parameter $D_m(A_p)$, the direct measurement of which is difficult for corroded plates. Nakai et al. [16] investigated the relation between D_m and DOP, where DOP may be measured via image processing of visual data from corroded surfaces when pits are sparsely overlapped, say up to 50% of DOP. The average corrosion diminution can also be estimated in terms of DOP as illustrated in Fig. 17. From this point of view, Yamamoto [6] discusses the random distribution of pitting corrosion in more detail. With all the necessary parameters estimated from DOP, Eqs. 26 and 30

Table 5 Locations of failure (sample 1)

DOP (%)	Age (year)	Max. pit depth (mm)	Location (*x*, *y*) of max. depth (mm)	Minimum sectional area (mm^2)	Location of min. sectional area *x* (mm)	Numerical failure point (*x*, *y*) (mm)	Experimental failure point (*x*, *y*) (mm)
19	5.0	1.444	(15.5, 12.5)	312.344	80.0	(81.0, 35.5)	(81, 35.5)
51	6.75	1.822	(15.5, 12.5)	306.006	38.5	(81.0, 35.5)	(81, 35.5)
73	7.75	2.006	(15.5, 12.5)	297.817	48.0	(81.0, 35.5)	–
92	9.5	2.293	(15.5, 12.5)	283.3742	48.0	(47.0, 26.0)	(47.0, 26.0)
99	13.0	2.779	(15.5, 12.5)	259.547	48.0	(47.0, 26.0)	–
100	17.0	3.501	(100.0 3.0)	235.97	48.0	(47.0, 26.0)	(47.0, 26.0)

The origin $x = y = 0$ is located at the lower left end of the processed area

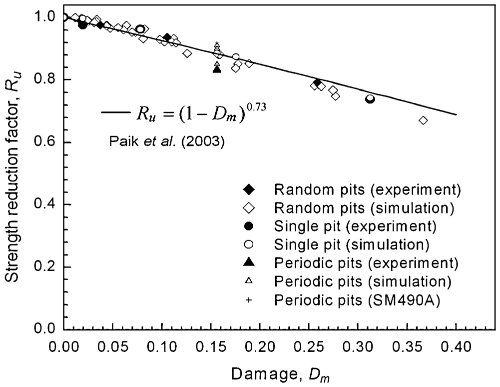

Fig. 23 The ultimate strength reduction factor, R_u, as a function of damage (steel A is used unless otherwise indicated)

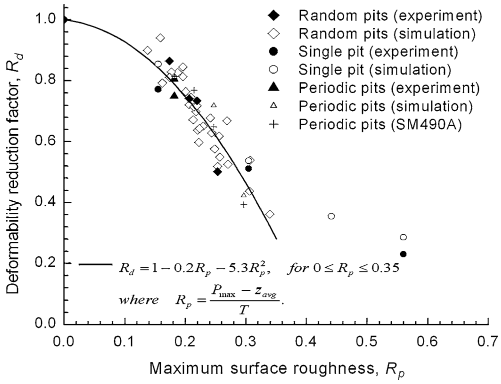

Fig. 24 The reduction of deformability, R_d, as a function of maximum surface roughness, R_p, of pitted plates under uniaxial tension (steel A is used unless otherwise indicated). $P_{\max}$ maximum pit depth, z_{avg} average corrosion diminution

can be evaluated. The practical applicability of Eq. 29 may rest on the possible estimation of the maximum pit depth in a plate.

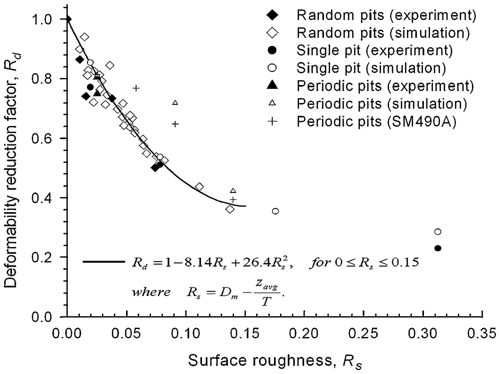

Fig. 25 The reduction of deformability, R_d, as a function of surface roughness, R_s, of pitted plates under uniaxial tension (steel A is used unless otherwise indicated)

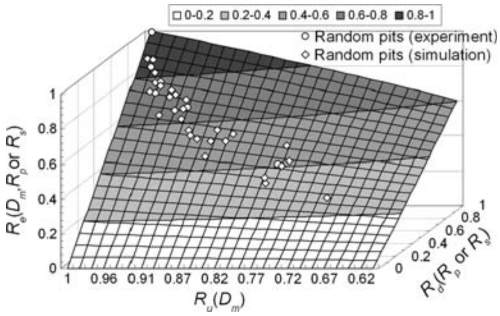

Fig. 26 The relationship among R_u, R_d, and R_e in a three-dimensional plot

6 General corrosion and its effect

6.1 Replica specimen and finite element model

In order to investigate the mechanical behavior of steel plate subjected to general corrosion, a steel plate (250 mm × 100 mm) was sampled from the bottom plate of an aged heavy oil carrier; the two surfaces of the sample

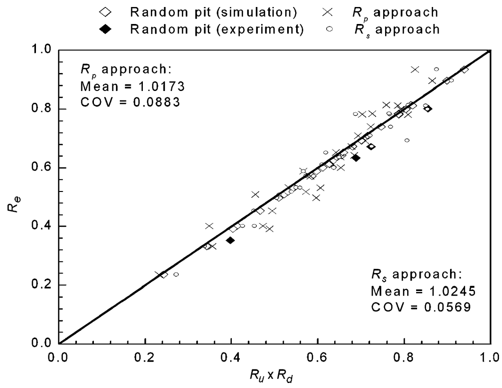

Fig. 27 The correlation of the reduction of energy absorption, R_e, and the simple estimate by ($R_u \times R_d$) for pitted plates, where four sets of data are plotted, i.e., the numerical simulation results, experimental results, and the results from the empirical formula (Eq. 31) using R_p or R_s to estimate the reduction of deformability

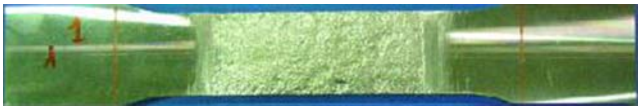

Fig. 28 Replica specimen of general corrosion

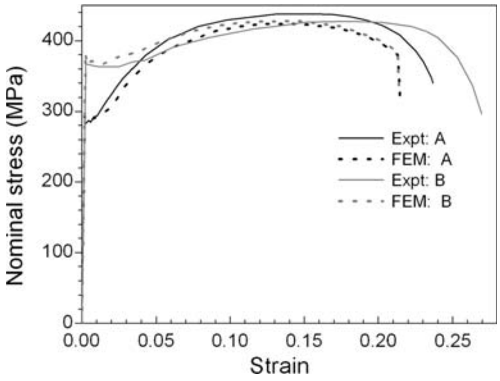

Fig. 29 Stress–strain curves of specimens with general corrosion

had been contacting heavy oil and seawater, respectively. The surface geometry of the sample plate was scanned at 0.5-mm intervals by a laser displacement sensor, and the results were stored as data for the CAD system. Based on the result of self-similarity [3], the replica specimen was reduced to 40% of the original size (100 mm × 40 mm), and the plate thickness before surface processing was 8 mm. The specimen surfaces were processed by a numerically controlled milling machine, and its surface was finished as shown in Fig. 28.

In the finite element analysis, both the top and bottom surfaces of the model have the corroded geometry. The three-dimensional finite element model consisted of 17040 elements. The element size in the processed area was 0.5 × 1 × 4 mm in the x, y, and z directions, respectively. The accuracy of the replica specimen and the finite element model was confirmed by comparing with the actual average corrosion diminution calculated by Eq. 25.

Table 6 Comparison of experimental results and empirically predicted values of general corroded steels

	Ultimate strength reduction factor, R_u	Reduction of deformability, R_d	Reduction of energy absorption, R_e
Steel A (experiment)	0.8537	0.8215	0.718
Steel B (experiment)	0.838	0.868	0.74
Present prediction	0.862[a]	0.8969[b]	0.7731[b]
Present prediction	0.862[a]	0.84217[c]	0.7259[c]

[a] Paik et al. [4]

[b] R_p approach, Eq. 29

[c] R_s approach, Eq. 30

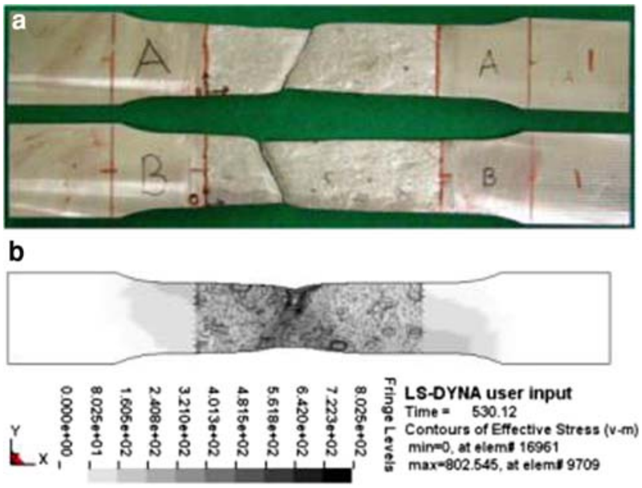

Fig. 30 Test and simulation models at failure. **a** Specimens of steels A and B after fracture, **b** von Mises stress just before fracture for steel A

6.2 Results and discussions

Figure 29 shows the nominal stress–strain curves obtained by experiment and numerical calculation for steels A and B. In all cases the strength reduction is in proportion to the average thickness diminution, while the deformability is slightly less than that of a flat plate (see Table 6). Failure occurs by pure shear deformation, which is followed by a cross diagonal shear band. In comparison with the experiments, shear deformation (slip) is less localized in the finite element analysis, so that the calculated deformability is slightly less than that seen in the experiments. Note that a plastic strain of 0.92 was set as the failure strain for the simulation of steel A with an element size 0.5 × 0.5 × 4 (mm). The fracture location is also shown in Fig. 30a, b. The failure occurs in the zone of maximum thickness diminution.

The reductions in strength, deformability, and energy absorption are approximated fairly well by Eqs. 26–31, as listed in Table 6, where the damage, D_m, was 0.1841, the DOP was 100%, the maximum diminution, P_{max}, was 2.282 mm, and the average diminution, z_{avg}, was 1.307 mm. With regard to the application of the proposed empirical formulae, since DOP is considerably high in the case of general corrosion, it is difficult to predict the average diminution, z_{avg}, and maximum pit depth, P_{max}, from DOP. Detailed thickness measurements are required to obtain these quantities in this case.

7 Conclusions

After the true stress–strain relationship was successfully measured using a vision sensor system, the strength and deformability of steel plates with randomly distributed pits and with general corrosion were investigated both experimentally and numerically. Two steels with yield ratios of 0.657 and 0.841 were used in this study to investigate their integrity in the corroded state. We may draw the following conclusions:

- After the average axial strain has been measured, the correction factor for the triaxial stress state can be estimated to obtain the true stress–strain relationship after the bifurcation.
- The fracture strain from the finite element analysis is properly calibrated to the mesh size.
- The strength reduction factor given by Paik et al. [4] is also applicable to the tensile strength reduction factor.
- The reduction in deformability and energy absorption capacity due to pitting corrosion and general corrosion under uniaxial tension can properly be estimated by the proposed empirical formulae.

Acknowledgments The authors express their earnest gratitude to Professors Y. Kawamura and T. Wada for their valuable suggestions and comments on this work, and thanks are extended to Mr. N. Yamamura, Mr. Y. Yamamuro, Mr. K. Shimoda, and Mr. S. Michiyama for their support. This work was supported by Grant-in-Aid for Scientific Research (A(2) 17206086) from the Ministry of Education, Culture, Sports, Science and Technology of Japan to Yokohama National University. The materials used for the experiments were specially processed and provided by the Nippon Steel Corporation. One of the authors, Md. M.A., is supported by a Japanese Government Scholarship. The authors are most grateful for these supports.

References

1. ISSC (2006) Committee Report V.6. Condition assessment of aged ships. In: Proceedings of the 16th international ship and offshore structures congress. University of Southampton, England, pp 255–307
2. Nakai T, Matsushita H, Yamamoto N, Arai H (2004) Effect of pitting corrosion on local strength of hold frame of bulk carriers (1st report). Mar Struct 17:403–432
3. Sumi Y (2008) Strength and deformability of corroded steel plates estimated by replicated specimens. J Ship Prod 24–3:161–167
4. Paik JK, Lee JM, Ko MJ (2003) Ultimate strength of plate elements with pit corrosion wastage. J Eng Marit Environ 217:185–200
5. Paik JK, Lee JM, Ko MJ (2004) Ultimate shear strength of plate elements with pit corrosion wastage. Thin Wall Struct 42:1161–1176
6. Yamamoto N (2008) Probabilistic model of pitting corrosion and the simulation of pitted corroded condition. In: Proceedings of the ASME 27th international conference of offshore mechanics and arctic engineering. Estoril, Portugal, OMAE2008-57623
7. Yamamoto N, Ikegami K (1998) A study on the degradation of coating and corrosion of ship's hull based on the probabilistic approach. J Offshore Mech Arct Eng 120:121–127
8. Bannister AC, Ocejo JR, Gutierrez-Solana F (2000) Implications of the yield stress/tensile stress ratio to the SINTAP failure assessment diagrams for homogeneous materials. Eng Fract Mech 67(6):547–562
9. Zang ZL, Hauge M, Ødegård J, Thaulow C (1999) Determining material true stress–strain curve from tensile specimens with rectangular cross-section. Int J Solids Struct 36:3497–3516
10. Scheider I, Brocks W, Cornec A (2004) Procedure for the determination of true stress–strain curves from tensile tests with rectangular cross-sections. J Eng Mater Technol 126:70–76
11. Bridgman PW (1964) Studies in large plastic flow and fracture. Harvard University Press, Cambridge
12. Ostsemin AA (1992) Stress in the least cross section of round and plane specimens. Strength Mater 24(4):298–301
13. Cabezas EE, Celentano DJ (2004) Experimental and numerical analysis of the tensile test using sheet specimens. Finite Elem Anal Des 40(5–6):555–575
14. Hallquist JO (2006) LS-DYNA theoretical manual. Livermore Software Technology Corporation, Livermore
15. Robert McNeel and Associates (2003) Rhinoceros user guide: NURBS modeling for windows. Version 3.0, McNeel, Seattle
16. Nakai T, Sumi Y, Saiki K, Yamamoto N (2006) Stochastic modeling of pitting corrosion and tensile tests with artificially pitted members (in Japanese). J Jpn Soc Nav Archit Ocean Eng 4(1200):247–255